Lidar sensor for Europa Clipper feasability study

Kees Kroep

September 1, 2016

Abstract

This document investigates the feasability of a lidar sensor based of performance requirements provided by NASA. The main focus of this study is both the required laser power and the resilience of the device against proton radiation. Other considerations include manufacturability, readout specifications and lens specifications. Based on the results of this study a design will be proposed. A radiation test is performed to increase the knowledge about the radiation resilience of the technology used in the proposed design. Based on these findings a design is proposed.

Contents

Introduction

The Europa Clipper is a planned mission by NASA to conduct detailed reconnaissance of Juliter;s moon Europa and investigate whether the moon could harbor condition suitable for life. To aid in the landing process, a lidar sensor is proposed. The functionaily of the lidar sensor is twofold. At hig altitudes, the Lidar sensor must operate in Altimetry Mode, and be capable to accurately measure the altitude of the device with respect to the surface of Europa. When the Europa Clipper gets closer to Europa, the lidar sensor must switch to a Hazard Detection Mode, where it scans the landing site on the surface of Europa to make a heightmap to pick a suitable landing spot and to aid the final stages of the landing process.

This study will investigate the feasability of such a lidar sensor. The focus will lie on required laser power to meet the required resollution, and the resilience of the device against proton irradiation.

Chapter 1 will state the relevant specifications as provided by NASA, and elaborate on the basic structure of the lidar sensor. Finally all assumptions used throughout the study will be listed. Chapter 2 will investigate design choices for the Altimetry Mode and make perdictions about the feasability of the proposed design. Chapter 3 will investigate design choices for the Hazaerd Detection Mode, with a larger emphasis on SPAD design and manufacturability. Chapter 4 will investigate the resilience against proton irradiation of the proposed technology by performing a radiation test with a proton beam. Finally ?? will summarize the study and list a preliminary specsheet for the proposed design.

Chapter 1

Requirements and Specifications

1.1 High level specifications

The radiation and mass, power and volume budget are listed in table 1.1 and table 1.2.

Table 1.1: Overview of radiation limitations

Radiation	
Total Integrated Dose in Silicon behind 100 mil Al spherical shell	500 krad

Table 1.2: Requirements for mass, power and volume

Mass, Power & Volume Budget	
Optical Head	<5 kg
Inside vault	<1 kg
Max cable length between optical head and electronics	2 m
Power	<50 W

The Lidar sensor features two operation modes: the Altimetry Mode, and the Hazard Detection Mode.

1.2 Altimetry Mode

Altimetry Mode is the first phase of the landing. During the Altimetry Mode, the Lidar sensor has to provide the altitude of the sensor in relationship to the surface op Europa. The requirements for the Altimetry Mode are listed in table 1.3

Table 1.3: Requirements for Altimetry Mode

Altimetry Mode	Threshold	Goal
Max acquisition Slant Range	5 km	8 km
Range Accuracy (3-sigma)	1%	0.10%
Update Rate	0.1 Hz	1 Hz

1.3   Hazard Detection Mode

During the Hazard Detection Mode a 3d map of the surface of Europa must be created around the landing place. The Hazard Mode is operational when the sensor is close enough to the surface of Europa. The requirements for the Hazard Detection Mode can be found in table 1.4

Table 1.4: Requirements for Hazard Detection Mode

Hazard Detection Mode	Threshold	Goal
Max range (altitude)	400 m	500 m
Min Operational Range (altitude)	5 m	1 m
Range Accurcay (3-sigma on final 3D map)	10 cm	5 cm
Ground Sample Distance (per pixel on 3D map)	10 cm	5 cm
Ground Area Coverage at max altitude	100 m x 100 m	125 m x 125 m
Time for 3D map creation	1 s	1 s

1.4   Overview

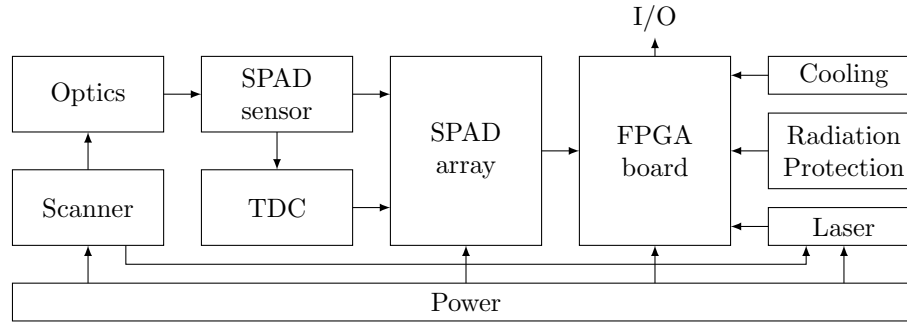A schematic overview of the sensor is shown in fig. 1.1.

Figure 1.1: Schematic overview

Laser: The laser must send short pulses but powerful pulses at a predefined frequency, to transmit photons that can be detected by the SPAD Sensor. A critical requirement for the laser is the amount of photons it is able to transmit as a function of time, within the budget and technical limitations.

SPAD Sensor: The Single Photon Avalange Diode (SPAD) is responsible for generating a digital pulse when hit by a photon. A circuit build around the SPAD must ensure that the sPAD is quenched as quickly as possible to minimize the deadline. A critical requirement for the SPAD is a small jitter to maximize the accuracy of the sensor.

TDC: The Time Interval to Digital Converter (TDC) is connected to the laser and the SPAD Sensor. The TDC must measure the time difference between the transmission of teh laser and the receiving at the SPAD sensor. This measurement requires an accuracy of tens of picoseconds to meet the accuracy requirements.

Scanner: The scanner handles the scanning motion that is needed to accumulate the entire picture. Different scanning motions can introduce undesired jitter and heavily influency the amount of SPAD Sensors that are needed on teh SPAD Array.

SPAD Array: The SPAD Array integrates the SPAD Sensors on a chip and connects them to the TDC's. The layout of the SPAD Array is closely rtelated to the scanning motion that is used in the scanner.

Optics: The optics must tranfer as much of the incomming photons as possible to the sensitive area on the SPAD Sensors. The Optics part also implements a bandpass filter around the target frequency.

FPGA Board: The FPGA Board controls the sensor. It is responsible for accumulating and interpreting the measurements from the TDC's, and controlling the Scanner and Laser.

Cooling: The cooling has to keep the temperature of the FPGA chip under a threshold temperature.

Radiation Protection: The Radiation Protection shields sensitive parts of the sensor from radiation. The most sensitive part of the system is expected to be the FPGA Board, based on experience.

Power: The power block has to supply the scanner, SPAD Array, FPGA Board, and the laser with the required power. The power block has to operate within the specified power budget.

1.5   Assumptions

This section will list the assumption that are made throughout the study.

Reflectivity of surface Europa: It is assumed that out of all light that hit's Europa, 35% is reflected in a perfectly diffuse manner.

Wavelength laser: The wavelength of light emitted by the laser is assumed to be $850\,nm$. This wavelength is a typcial choice for Silicon SPAD's. The main reason for this wavelength as opposed to $550\,nm$ is because the that sunlight is less strong in that region, and less background noise will lft after applying a narrow bandpass filter.

Bandpass filter:A bandpass filter will be used o filter background noise. This filter is assumed to be a bandpass filter with a center frequency of $850\,nm$ and a FWHM of $10\,nm$.The minimum transmission of the filter is 50%. These values are directly taken from the "*850nm, 10nm FWHM, 12.5mm Mounted Diameter*" product made by Edmund Optics and sold for 75 $.

Jitter of SPAD Sensor: The jitter of the SPAD Sensor, or Full Width Half Max (FWHM) is assumed to be $100\,ps$. This value is a typical FWHM for state of the art Silicon SPAD's.

Jitter of TDC: The jitter of the TDC's is assumed to be insignificant when compared to the jitter of $100\,ps$ caused by the SPAD Sensors. Experience with previous designs show that TDC jitter is generally a very small contributor to overall jitter.

Resolution of TDC: The accuracy of the TDC is assumed to be $50\,ps$.

Sunlight: It is assumed that the light from the sun that is reflected of Europa is the only signifant contributor to background noise. No other sources of light will be considered.

Photon Detection Probability: It is assumed that the PDP of the SPADs is 10%.

Laser light hitting target: It is assumed that all the light that leaves the laser is hitting the target area on Europa.

Laser efficiency: It is assumed that the laser has an efficiency of 10%.

Chapter 2

Altimetry Mode

The Altimetry Mode is the mode in which only the altitude of the device in relationship to Europa is required. The main challenges for the altimetry mode are acquiring the required resolution, acquiring the required speed, staying within the power budget, and being sufficiently resilient against the accumulated radiation for the entire trip.

The first step will be to create a model of the noise that will be present at Europa. Then the required amount of signal will be calculated, resulting in the required signal power.

2.1 Optics

The receiver optics are a good place to start of with, beacuse the optics are not very dependent on results attachieved in other areas. The optics have to transport as many desired photons, and as little unwanted photons to the active area on the SPADs as possible. All while having an acceptable depth of field.

The most basic solution is a single lens with an aperture. The opacity of the lens can be calculated with the absorption of the lens material and f-number of the lens using eq. (2.1).

$$\text{opacity} = \frac{1 - \text{absorption}}{\text{f-number}^2} \tag{2.1}$$

The performance of a possible configuration is shown in table 2.1

Table 2.1: Performance of basic optics solution

Basic Optics	
f-number	2.00
absorption	5.00 %
opacity	23.75 %

2.1.1 Improvements

There are a couple of additions that can improve the performance of the optics. The first and very necessary one, is the use of a bandpass filter. The transmitted signal will have a very specific bandwidth of $850\,nm$. Using a narrow bandpass filter one can filter out an enormous part of the background noise. The filter will have an opacity of $50\,\%$ for the target wavelength.

The captured photons that hit the lens need to be guided to the active area of the SPADs. If the active area on the chip is very small, one can use microlenses to improve the effectiveness of the optics. A Microlens focusses light on a single SPAD on the chip. Two types of microlenses will be considered: a spherical lens, and a square shaped lens. The presence of microlenses poses

a limitation of the main lens. The f-number must be relatively large. A higher f-number means a smaller aperture and therefore more loss of photons. A way of dealing with this problem is to use a second lens instead. An overview of the available options is shown in fig. 2.1
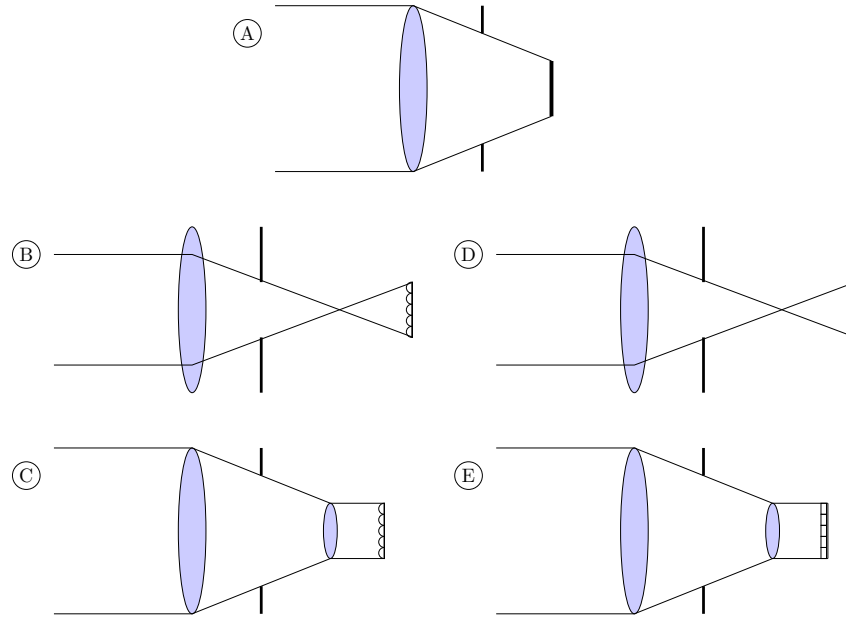

Figure 2.1: Overview of possible receiver optics implementations

$$\text{opacity} = (1 - \text{absorption}_1)(1 - \text{absorption}_2) \cdot \text{opacity filter} \cdot \frac{X}{\text{f-number}^2} \tag{2.2}$$

Where X is the active area on the chip. A comparison between the different options is shown in table 2.2

Table 2.2: comparison of different optics solutions

Type	A	B	C	D	E
absorption 1st lens	0.05	0.05	0.05	0.05	0.05
f-number	2	8	2	8	2
absorption 2nd lens	0	0	0.05	0	0.05
opacity bandpass filter	0.5	0.5	0.5	0.5	0.5
active area on chip	X	0.55	0.55	0.65	0.65
effective opacity	$X \cdot 11.75\,\%$	$0.4082\,\%$	$6.204\,\%$	$0.4924\,\%$	$14.6656\,\%$

The comparison in table 2.2 shows some good alternatives to the basic lens, if there is a need for it due to a small active area on the chip. However, most of the future calculations will focus on the basic model A.

2.2 Noise caused by the sun

The sun is the most dominant source of unwanted photons at Europa. This section will investigate how much energy is hitting the surface of Europa.

To calculate that the sun will be modelled as an ideal black body. The spectral irradiance of the sun can be calculated using eq. (2.3).

$$I_\lambda(\lambda, T) = \frac{2hc^2}{\lambda^5} \frac{1}{e^{\frac{hc}{\lambda kT}} - 1}$$

(2.3)

where $I_\lambda(v, t)$ is spectral irradiance with unit W/m^3.
h is the planck constant
c is the speed of light in vacuum
k is the Boltzman constant
λ is the wavelength of the electromagnetic radiation
T is the absolute temperature of the body

The spectral irradiance of the sun is calculated in table 2.3.

Table 2.3: Calculation of sun irradiation

Sun irradiation	
h	$6.63 \cdot 10^{-34}\, Js$
c	$3.00 \cdot 10^{8}\, m/s$
k	$1.38 \cdot 10^{-23}\, j/K$
λ	$850.00\, nm$
T	$5.78\, kK$
I_λ	$1.51 \cdot 10^{4}\, W/m^2/nm$

The next step is to calculate the power emitted by the sun in the specified bandwidth, at the location of Europa. The specified bandwidth is in this case the assumed bandpass filter used on the lens. The emitted power is calculated by modelling the sun as a point source, and then spreading that power over a sphere with a radius equal to the distance between the sun and Europa, as is done in eq. (2.4).

$$P_{sun} = I_{\text{sun}} B_\lambda S \frac{r_{\text{sun}}^2}{r_{\text{europa}}^2}$$

(2.4)

where I_{sun} is the spectral irradiance of the sun at the center frequency of the filter, B_λ is the bandwidth of the filter in meters, S the surface area of the target area on Europa, r_{sun} the of radius of the sun, and r_{europa} the distance between Europa and the sun. The effective radiance of the background noise at Europa is calculated in table 2.4 using eq. (2.4).

Table 2.4: Calculation of background power on target area on Europa

Background power	
I_λ	$1.51 \cdot 10^{13}\, W/M^3$
B_λ	$10.00\, nm$
Surface area	$15625.00\, m^2$
r_{sun}	$6.96 \cdot 10^{5}\, km$
r_{europa}	$7.79 \cdot 10^{8}\, km$
P_B	$1.89\, kW$

The next step is to calculate the percentage of energy that hits the device when hovering over Europa. The focal length and aperture of the lens will be configured in such a way that the target surface on Europa fills the entire view at the maximum altitude of the Hazard Detection Mode, so that altitude will be chosen to calculate the received noise power. The amount of power received at the lens of the device can be calculated using eq. (2.5).

11

$$P'_B = \frac{P_B \cdot R_{Europa} \cdot D_l \cdot \text{opacity}}{2r^2} \tag{2.5}$$

where P'_B is the power hitting the lens,
P_B the noise power on the target area of Europa,
R_{Europa} the reflectivity of Europa,
D_l the diameter of the lens,
opacity the opacity of the lens,
and r the altitude of the device. The calculations are performed in table 2.5.

Table 2.5: Amount of noise power that hits the SPAD array

noise power at SPADs	
P_B	$1.89\,kW$
r	$500.00\,m$
R_{europa}	$35.00\,\%$
Diameter lens (D_l)	$50.00\,mm$
opacity optics	$11.75\,\%$
P'_B	$7.76\,\mu W$

Finally the power needs to be converted to number of photons. To calculate how many photons bounce from the surface of Europa and actually hit the light. To calculate the amount of photons one needs to know the amount of energy per photon. This can be calculated using eq. (2.6). The calculation is performed in table 2.6.

$$E_{photon} = \frac{hc}{\lambda} \tag{2.6}$$

Table 2.6: calculation of photon energy at the specified wavelength

energy of photon	
h	$6.63 \cdot 10^{-34}\,Js$
c	$3.00 \cdot 10^{8}\,m/s$
λ	$850.00\,nm$
E_{photon}	$2.34 \cdot 10^{-19}\,J$

The amout of photons per second can then be calculated using eq. (2.7). The calculation is shown in

$$\text{photon}/s = \frac{P}{E_{photon}} \tag{2.7}$$

Table 2.7: calculation of amount of photons that hit the SPAD array per second

photons hitting SPADs	
P'_B	$7.76 \cdot 10^{-6}\,W$
E_{photon}	$2.34 \cdot 10^{-19}\,J$
photons at SPADs	$3.31 \cdot 10^{13}\,\text{counts'}/s$

2.3 Detected photon characterisation

This section tackles the problem of calculating the resolution of the set-up. To do this, the different types of detection by the SPADs, due to sunlight, signal source and dark counts, must be characterized first.

To avoid pileup a couple of temporary assumptions about the performance of the SPADs will be made. Firstly, it is temporarily assumed that the percentage of the surface that is sensitive to photons is $50\,\%$. Secondly it is temporarily assumed that the dark count rate (DCR), of the entire array is $PSS_N = 1 \cdot 10^9 \text{photon}/s$.

The amount of detected sunlight photons detected by the SPADs per second can now be calculated using eq. (2.8). The calculation are shown in table 2.8. Both the sunlight detections and the DCR detections are uniformly distributed.

$$PPS_B = \text{photons at SPADs} \cdot \text{PDP} \cdot \text{effective area} \tag{2.8}$$

Table 2.8: Amount of detected sunlight photons detected per second

PPS for background photons	
Photons at SPADs	$3.31 \cdot 10^{13}\ \text{photon}/s$
PDP	$10.00\,\%$
effective area	$50.00\,\%$
PPS_B	$1.66 \cdot 10^{12}\ \text{counts}/s$

The next step is to characterize the relationship between the laser power and the received photons. It is assumed that all light emitted by the laser is hitting Europa. It is also assumed that the efficiency of the laser is $10\,\%$. Next, similar calculation as performed with P_B can be used to calculate the amount of detected signal photons per second PPS_S. There is one important difference however: where for sunlight an altitude of $500\,m$ was used, for the signal photons an altitude of $8\,km$ must be considered. The calculation are performed in table 2.9. Note that even with the largest power budget of $50\,W$, the SNR will be well below $0\,dB$.

Table 2.9: Amount of detected signal photons detected per second

PPS for background photons	
P_S	$1.00\,W$
Altitude	$8.00\,km$
P'_S	$1.61 \cdot 10^{-11}\,W$
PPS_S	$3.43 \cdot 10^6\ \text{counts}/s/W$

The signal photons are not uniformly distributed like the noise and background photons. The signal photons are assumed to be distributed in a normal distribution with a $FWHM = 100\,ps$. This distribution is convoluted with the jitter on the SPADs, which is assumed to be a normal distribution with a $FWHM = 100\,ps$. Using eq. (2.9) and eq. (2.11), the resulting distribution has a $\sigma_S = 60\,ps$. The mean μ_s is equal to the time of flight of the photon.

$$FWHM = 2\sqrt{2\ln 2}\,\sigma \tag{2.9}$$

$$\sigma = \frac{FWHM}{2\sqrt{2\ln 2}} \tag{2.10}$$

$$\sigma_{f\otimes g} = \sqrt{\sigma_f^2 + \sigma_g^2} \tag{2.11}$$

The maximum allowable $FWHM$ of the measurement is $333\,ps$ as shown in section 1.5. Using eq. (2.10) the maximum standard deviation is $\sigma = 141\,ps$.

2.4 Sampling Method

The sampling method used has a massive impact on the performance of the system. This section investigates the options that can be chosen from.

The time that the sensor should listen to a response is determined by the maximum round trip time of a photon, and can be calculated using eq. (2.12).

$$t_{round} = \frac{2r}{c} \tag{2.12}$$

where $c \approx 3 \cdot 10^8$ is the speed of light, and r the altitude of the sensor.

The next step is to calculate the relationship between oberved number of good and bad photons for a given listening period, and the resulting standard deviation of the measurement. To calculate the standard deviation of the sum of multiple random variables that are statistically independent, one can use eq. (2.13)

$$\text{Var}[aX + bY + cZ] = a^2\text{Var}[X] + b^2\text{Var}[Y] + c^2\text{Var}[Z] \tag{2.13}$$

Because the DCR and sunlight photons have the same uniform distribution they are taken from the same uniform random variable N, where n is the amount of detected sunlight and dark photons, $\mu_n = \frac{1}{2}t_{round}$, and $\sigma_n = \frac{1}{\sqrt{12}}t_{round}$. The signal photons are taken from the random variable S, where s is the amount of detected signal photons, $\mu_s = ToF$, and $\sigma_s = 42.5\,ps$. The resulting mean μ_{tot} can be calculated using eq. (2.15). The error with the desired μ can be calculated using eq. (2.17).

$$\mu_{tot} = \frac{1}{s+n}\left(\sum_{k=1}^{s}\mu_s + \sum_{l=1}^{n}\mu_n\right) \tag{2.14}$$

$$= \frac{s \cdot Tof}{s+n} + \frac{n \cdot \frac{1}{2}t_{round}}{s+n} \tag{2.15}$$

$$\mu_{error} = |ToF - \mu_{tot}| \tag{2.16}$$

$$= \left|\frac{n(ToF - \frac{1}{2}t_{round})}{s+n}\right| \tag{2.17}$$

The resulting standard deviation σ_{tot} can be calculated using eq. (2.21).

$$\text{Var}_{tot} = \text{Var}\left[\frac{1}{s+n}\left(\sum_{k=1}^{s}\text{Var}_s + \sum_{l=1}^{n}\text{Var}_n\right)\right] \tag{2.18}$$

$$= \frac{1}{(s+n)^2}(s\sigma_s^2 + n\sigma_n^2) \tag{2.19}$$

$$\sigma_{tot} = \sqrt{\text{Var}_{tot}} \tag{2.20}$$

$$= \frac{\sqrt{s\sigma_s^2 + n\sigma_n^2}}{s+n} \tag{2.21}$$

Using eq. (2.21), one can calculate the relationship between the amount of signal photons needed for a given amount of noise photons. For the long distance a $t_{round} = 53.3\,\mu s$ is used. Using

14

eq. (2.23) the realtionship between the number of noise photons and required signal photons is shown in fig. 2.2. Note that the amount of required signal photons first rises quickly, then slowly, and finally even drops. The reason for this trend is that increasing the number of random samples also decreases the standard deviation by itself. Figure 2.3 shows the same relationship for a smaller number of noise photons.

$$\sigma_{tot} = \frac{\sqrt{s\sigma_s^2 + n\sigma_n^2}}{s + n} \tag{2.22}$$

$$s = \frac{\sigma_s^2 + \sqrt{\sigma_s^4 - 4\sigma_s^2\sigma_{tot}^2 n + 4\sigma_n^2\sigma_{tot}^2 n} - 2\sigma_{tot}^2 n}{2\sigma_{tot}^2} \tag{2.23}$$
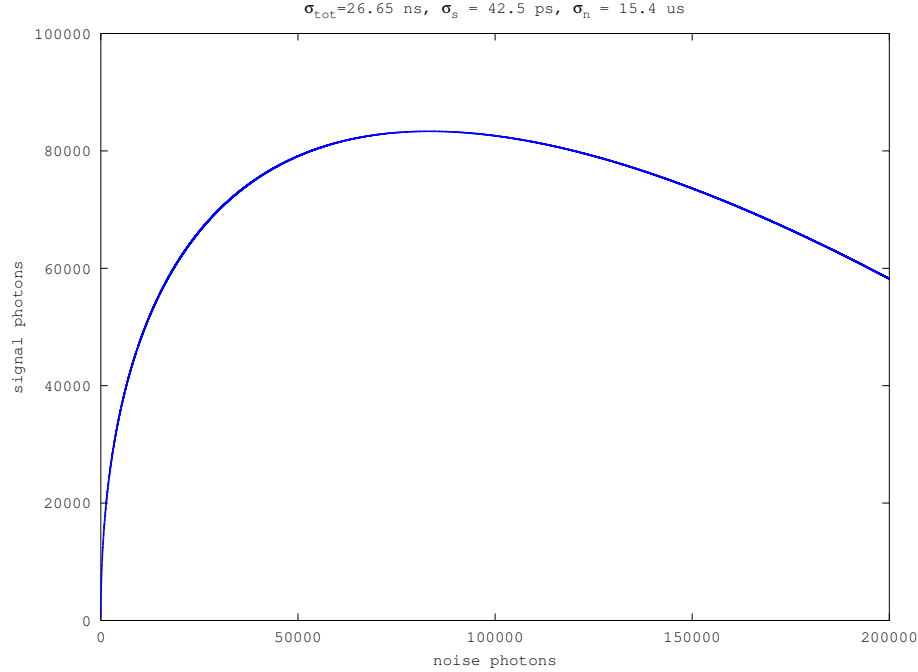

Figure 2.2: Relationship between number of signal and noise photons to get the required resolution

2.4.1   Intensity Threshold

An intensity threshold can be a very powerful way to improve signal to noise ratio. The signal photons all arrive with a $FWHM = 100\,ps$, while the noise photons are spread out over $53.3\,\mu s$. An intesnity threshold is a perfect way to take advantage of this. When the phoons are divided over bins, the expected number of bins can be modelled as Poission process. Using this the efficiency of the intesnity threshold can be perfomed which is shown in fig. 2.4, where the opacity is 1 if all photons pass through the threshold, and 0 if no photons pass through the threshold. It is important to notice that a certain threshold has no effect at all if the expected number of photons is sufficiently high. The threshold is most effective when the opcity for the signal photons is close to 1, and the opacity for noise photons close to 0. To apply a threshold however, one needs to assemble a historgram of all the detections. The feasability of such a histogram will be investigated later, but for now both a system with and without an intesnity threshold are considered.
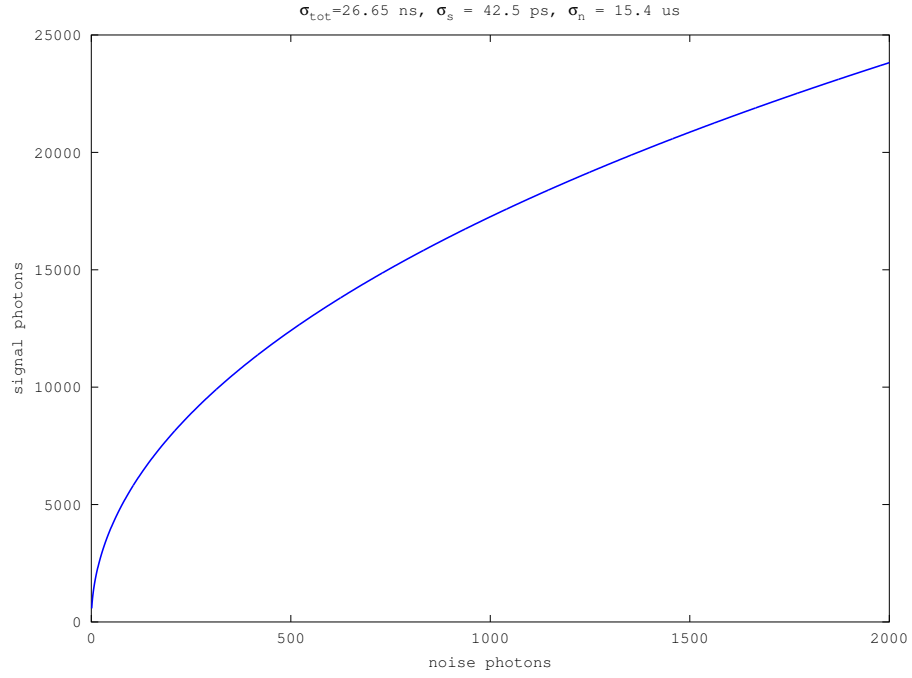
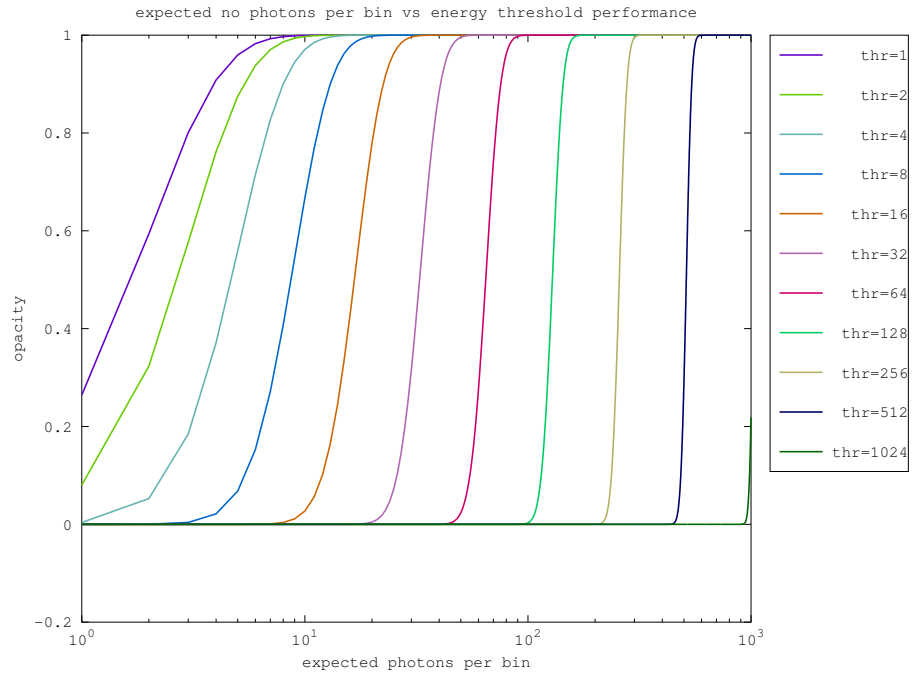Figure 2.3: Relationship between number of signal and noise photons to get the required resolution

Figure 2.4: Expected number of photons per bin versus the opacity of the threshold, where opacity=1 means all photons pass through the threshold, and opacity=0 means no photons pass through the threshold

16

2.5 Required Laser Power

The requirement for the altimetry mode changes based on the height. The target is a resolution of at least 0.1%. To ensure that this requirement is met, both the largest altitude of $8\,km$, and the smallest altitude of $500\,m$ will be investigated.

The minimum resolution for the largest and shortest altitude are $8\,m$ and $0.5\,m$ respectively. The maximum allowable FWHM can be calculated using eq. (2.24). Using eq. (2.10) the maximum standard deviation can be calculated. The calculations are performed in table 2.10.

$$FWHM_{max} = \frac{2x}{c} \tag{2.24}$$

Table 2.10: Required standard deviation to meet the system requirements

AM requirements	short	long
altitude	$500\,m$	$8\,km$
resolution	$50\,cm$	$8\,m$
FWHM	$3.33\,ns$	$53.33\,ns$
σ	$1.42\,ns$	$22.65\,ns$

2.5.1 Peak Power

A very important restriction to the sampling method is the highest achievable peak power of the laser. If there would be no limit on the peak power, one could send out one extremely powerful pulse, listen for an extremely short period of time, and then reconstruct the altitude. The key advantage is the listening time. Shortening the listening time directly reduces the amount of background and noise that can be observed.

During the transmission of the laser, the peak power must be more than the average power of the background noise. Using eq. (2.25) one can calculate the average optical power required for the laser to get an $SNR = 0$. These calculations are performed in **??**. Combing that result with a laser efficiency of 10%, this gives a required electrical power of $4.8\,MW$ to match the power of the sun. In order to be able to distinguish noise from signal, the peak power is lower bound by this amount of power.

$$P_{av} = P_B \frac{\text{HDM altitude}^2}{\text{current altitude}^2} \tag{2.25}$$

Table 2.11: required average power to get SNR=0

matching average power	
P_B	$1.89\,kW$
HDM altitude	$500\,m$
current altitude	$8\,km$
P_{av}	$482.78\,kW$

Using the results in fig. 2.2, and the calculations performed in **??**, a relationship between the peak power and average power can be constructed, which is shown in fig. 2.5. This figure illustrates the clear advantage of having a high peak power. If the peak power is high enough, a single pulse is enough to acquire the desired resolution, resulting in an extremely low average power. The figure also shows that the increase of amount of pulses decreases the required peak power, but after a
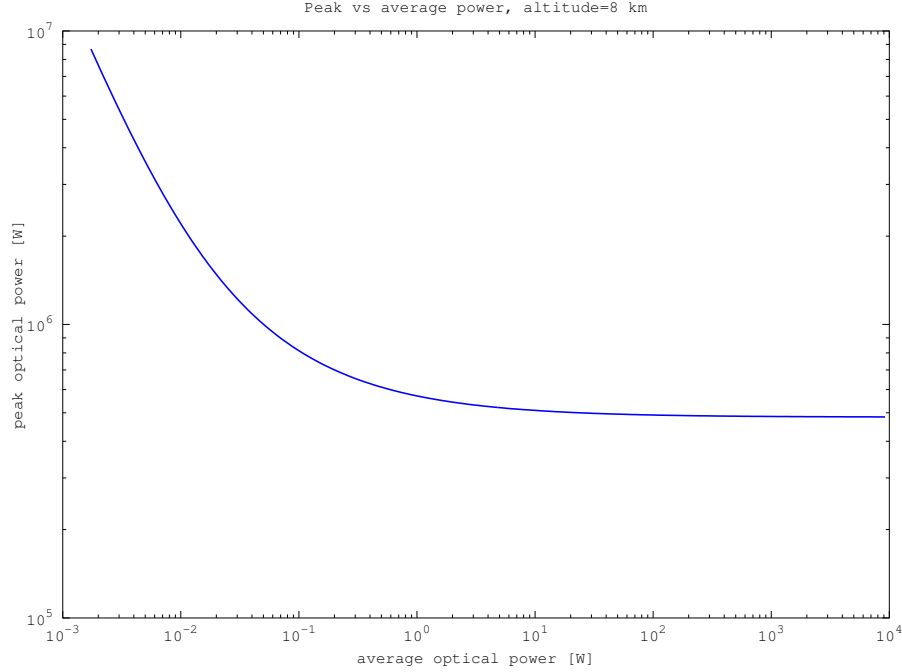
Figure 2.5: required peak power for a given average power for the requirements at an altitude of $8\,km$

certain point this decrease is no longer significant. It is important to note that the variation in the mean is not considered here, which means that the actual required power will higher.

When the energy threshold is added a very different relationship can be found. The threshold can be so powerful that noise can be almost completely eliminated without losing any signal photons, as long as the difference between the expected number of signal photons per bin is sufficiently larger than the expected number of noise photons per bin. To avoid pileup, it is assumed that a difference of a factor $F = 10$ will be sufficient. It will also be assumed that a single pulse will be enough to acquire the required information. One can now calculate that the peak optical power must be at least $4.8\,MW$. This is also an enourmous amount of peak power to produce, and hardly feasable.

2.5.2 Reducing the field of view

The limit calculated in **??** is too high to design feasable laser specifications. The only way to reduce this lower limit, the amount of observed background noise must be further limited. To limit the amount of observed background noise, the field of view must be limited. Until this point the amount of background noise was defined as the amount of noise hitting the device from a $125 \times 125\,m^2$ surface on Europa at an altitude of $500\,m$. This means that on an altitude of $8\,km$, a surface of $2 \times 2\,km$ is observed. Now we take a look at what happens when the field of view is limited to a thin slice of $125 \times 0.1\,m^2$. Assuming that the laser is capable of tranmitting exactly into the small target area, this reduces the limit calculated in **??** by a factor 1250. This shows that the altimetry mode for the laser is feasable, but that a sufficiently limited field of view is required. The target area for the Altimetry Mode can be arbitrarily small. The field of view can be limited by either the lens, or by disabling a portion of the SPADs on the chip.

Chapter 3

Hazard Detection Mode

The Hazard Detection Mode is the mode of operation that operates closer to Europa than the Altimetry Mode. The main difference and challenge is however, is that this time a detailed heightmap must be formed. Therefore, for the Hazard Detection Mode, the layout of the SPADs and the scanning method are essential in determining the feasability of the device.

3.1 Types of SPADs

In Hazard Detection Mode, individual SPADs will have the responsibility of measuring their part in the target. Therefore it is important to first investigate what type of SPAD is best suited for the device. As mentioned in section 2.1, SPADs can have microlenses. Two types are considered: conventional spherical lenses, and rectangular lenses. Spherical lenses typically achieve an effective active area of approximately 55 %, while rectangular lenses typically get an effective active area of appeoximately 65 %. These approximations are based on the work of Pavia et al. [4]. The active area can also be shaped in different sizes, and a circular and rectangular shape are considered here. An overview of the different options is shown in fig. 3.1. The work of Pavia et al. was used for the
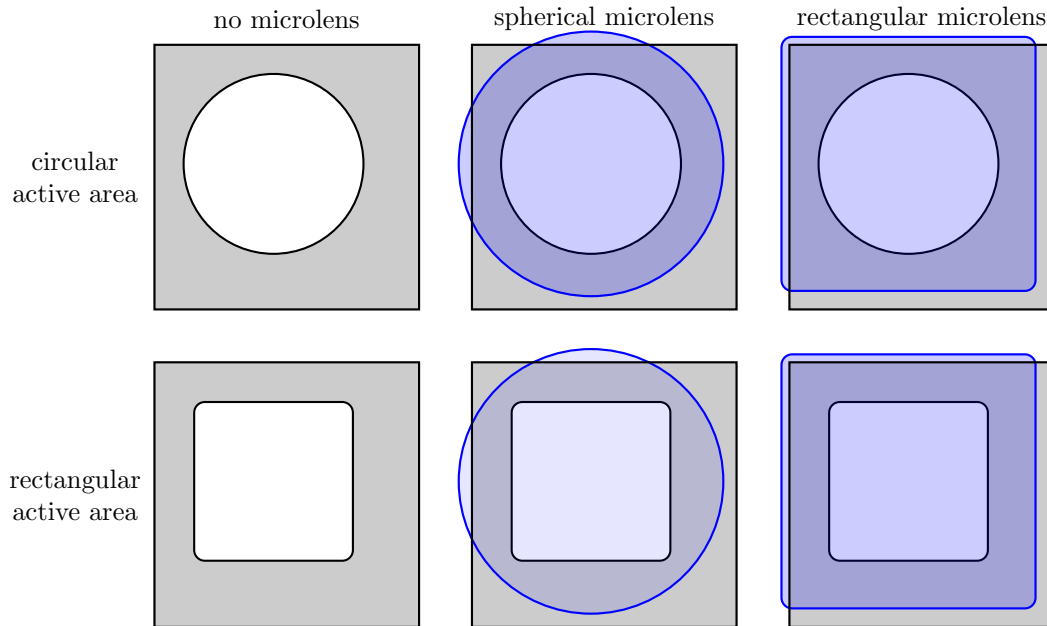

Figure 3.1: Options for lenses with varying types of active areas and microlenses

19

The use of microlenses is not the only viable of option of increasing the active area on the chip. A second option is to pick the circuitry required per SPAD, and push it to the side. These circuitry include the Read-Out Integrated Circuit (ROIC) that also includes the quenching of the SPADs, and the Time interval to Digital converter (TDC). It is important to note that the push-out of the circuitry poses additional constraints of the design. The pushed out electronics must still be in a reasonable close range to the SPADs, which limits the dimensions of a device using push-out electronoics.

To avoid pileup, the following calculations are done for an $0.18\,\mu m$ technology and it is assumed that the ROIC will take up $110\,\mu m^2$ surface area per SPAD, and that the TDC will take up $1200\,\mu m^2$ surface area per SPAD. It will also be assumed that the minimum amount of pitch between two SPADs is $1.5\,\mu m$. These numbers are based on current SPAD designs in $0.18\,\mu m$ technology. An overview of the performance of all different possibilities is shown in fig. 3.2. Note that, while the microlensen are assumed to focus the light on an arbitrarily small area, this is in reality not the case. If one would use no push-out electronics with a microlens for example, the pitch must be at least $40\,\mu m$ because otherwise there will not even be active area to focus the light on.
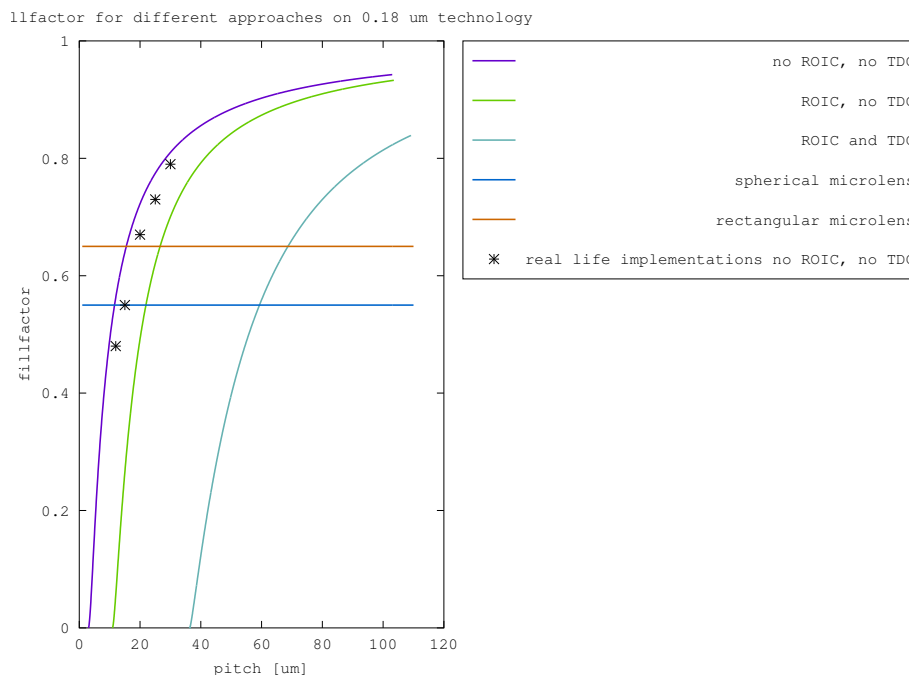

Figure 3.2: Fillfactor for different approaches in relationship to the pitch of the SPAD on $0.18\,\mu m$ technology

3.2   Scanning motion

The specifications indicate a target area of $125 \times 125\,m^2$ with a ground sample distance of $5\,cm$. This results in 2500×2500 pixels. For now however an array of 2048×2048 pixels will be considered, because that is a more convenient power of 2. Depending on the SPAD layout, different scanning motions arerequired to cover the target area. Possible scanning motions for different SPAD array configurations are shown in fig. 3.3. Note that the 2048×1 motion is in essense a special case of the $2048 \times N$ motion, where exactly one row of pixels is observed at a time. 2048×2048 is also a special case of $2048 \times N$ where no scanning motion is needed. The $M \times N$, with $M < 2048$ and $N < 2048$ needs a scanning motion in both x and y direction. This makes the scanning motion very

complicated and unreliable. Therefore only the family of solutions with $2048 \times N$ will be considered.
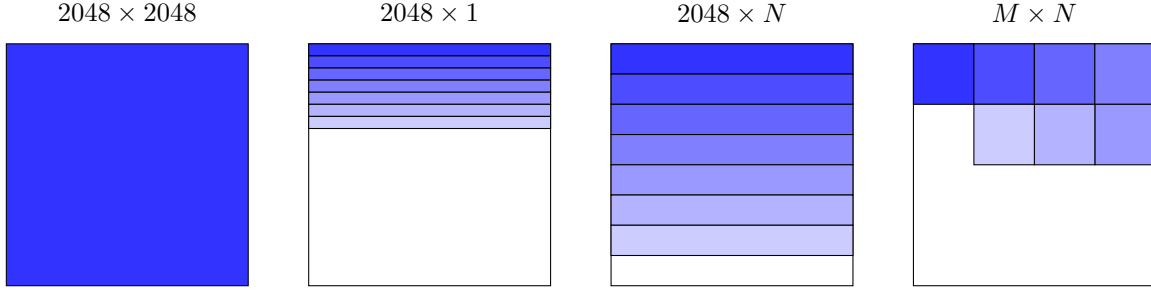

Figure 3.3: Different types of scanning motions

3.3 SPAD layout

The results in fig. 3.2 clearly show that an increase in the pitch will also increase the part of the SPAD that is active. However, arbitrarily large pitches cannot be afforded. An array of 2048×2048 does not allow for push-out electronics. Therefore the minimum pitch is $40\,mum$ combined with a microlens. This amount of pixels would result in a chip area of $8 \times 8\,cm^2$ which is not feasable with current manufacturing technology. This means that with current technology constraints a 2048×2048 SPAD array cannot be manufactured and is therefore not feasable. In fact, even in a single dimension, $8\,cm$ is not feasable. This means that push-out electronics of at least the TDC are a requirement to meet the pixel density requirements.

The push-out electronics pose a restriction that the electronics must be at most 4, or in extreme cases, 8 SPAD pitches away from the SPAD. This restricts the SPAD array to a maximum of 2048×8 pixels. To avoid pileup, only the feasability of a pitch of $20\,\mu m$ will be investigated. Using the results obtained in fig. 3.2, one can see that the effectiveness of a SPAD with push-out ROIC is approximately $75\,\%$ and the effectiveness of a SPAD with onboard ROIC approximately $55\,\%$. The surface area of the SPAD array is a line with a length of $4\,cm$ and a width of atleast $160\,\mu m$. There is no point in using microlenses for these dimensions. They add little to no benefit on the efficiency, and there are several issues with the use of microlenses, like restrictions on the lens, that can't make them justifiable in this setup. To avoid pileup, the feasbility of a SPAD array of 2048×8 will be considered.

3.4 Detected photon characterisation

This section is similar to section 2.3, but recalculates parts that are different for the HDM mode. First of all, the results of all the SPAD measurements are no longer bundled together, but interpreted seperately. Also the device is a lot closer to Europa with an altitude of at most $500\,m$ which causes the laser to be me more effective when compared to the noise. The new values to work with are shown in table 3.1. Note that the PPS_S is the amount of photons per Watt of optical transmitted energy.

Table 3.1: Amount of backgroun (B), dark count (N), and signal (S) counts that are observed by a single SPAD per second

photons per SPAD	
PPS_B	$3.95 \cdot 10^5$ counts$/s$
PPS_N	$2.00 \cdot 10^3$ counts$/s$
PPS_S	$5.36 \cdot 10^4$ counts$/s/W$

Another important changed property, is that the maximum time of flight $t_{round} = 3.33\,\mu s$. This directly means that per measurement, less noise is received. However, the expected amount of noise per bin remains the same. The new $\mu_n = \frac{3.33 \cdot 10^{-6}}{2} = 1.67\,\mu s$, and the new $\sigma_n = \frac{3.33 \cdot 10^{-6}}{\sqrt{12}} = 304\,ns$.

3.5   Required laser power

The laser power too requires new calculations when compared to those performed in section 2.5. First and foremost, the resolution required for the Hazard Detection Mode is $5\,cm$, with a resulting maximum allowable standard deviation of $\sigma_{tot} = 142\,ps$. Finally, it was decided that a scanning method would be used where the target area would be divided into at least $2048/8 = 256$ pieces. Figure 3.4 and fig. 3.5 show the updated relationship between signal and noise photons to meet the requirements.
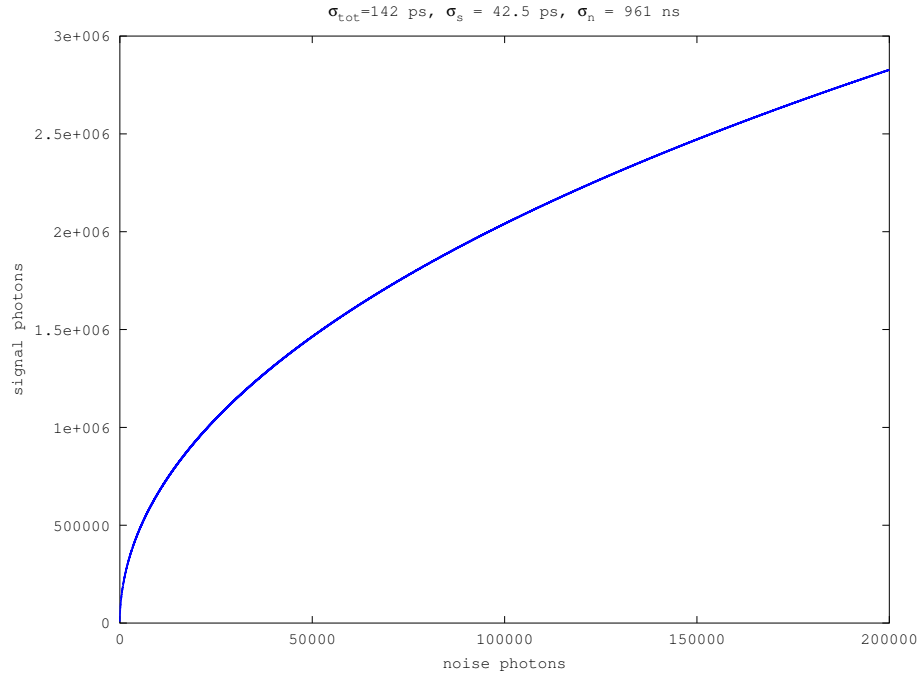

Figure 3.4: required signal photons for a given number of noise photons to meet the HDM requirements at maximum altitude

All the acquired new information can now be used to calculate a new relationship between the required peak power and average power. Note that in this case the least amount of pulses is 256. The reason being oly a 1/256th of the target can be observed at a time. The results of these calculations are shown in fig. 3.6. This time increasing the number of pulses does decrease the required signal power significantly. The more important result is however, that the power budget is orders of magnitude of for obtaining a feasable peak optical power for the laser. Therefore the HDM modus is not feasable without extra processing like an energy threshold.

The next step is to look at the energy threshold again. The average noise power $P_B = 7.4\,W$. In order to make sure that the expected amount of photons per bin is 10 times higher than for the noise, one needs a peak power of $P_{peak} = 74\,W$. The resulting average optical laser power is calculated below.
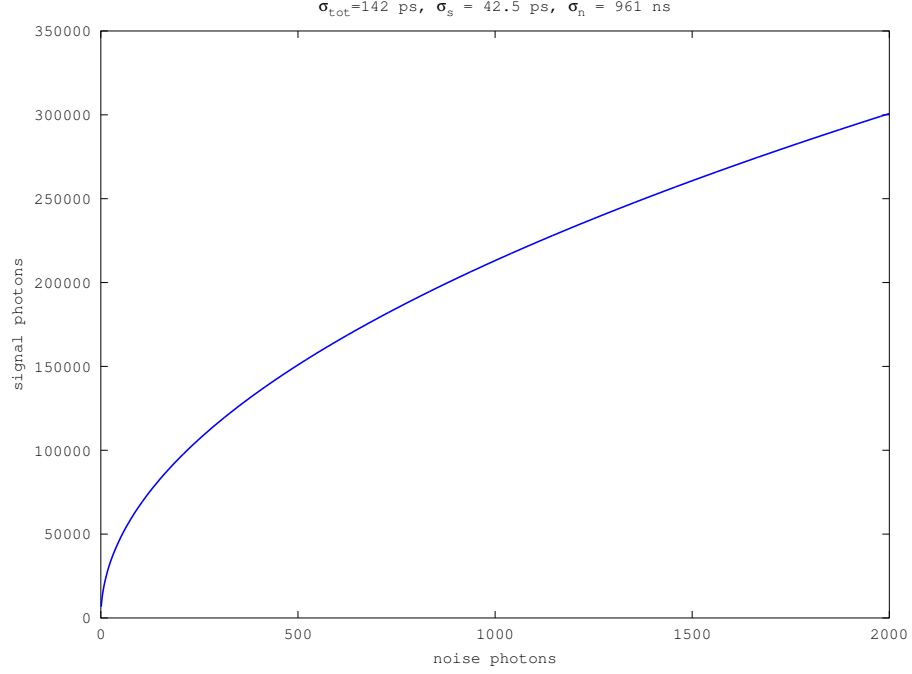
$\sigma_{tot}=142\ ps,\ \sigma_s = 42.5\ ps,\ \sigma_n = 961\ ns$

Figure 3.5: required signal photons for a given number of noise photons to meet the HDM requirements at maximum altitude

$$P_{av} = P_{peak} \cdot \frac{2048}{8} \cdot FWHM$$
$$= 74 \cdot 256 \cdot 100 \cdot 10^{-12}$$
$$= 1.89\,\mu W$$

Both the peak and average laser power fall royally in the power budget. This means that the device can meet the resolution requirements within the power budget, granted that the damage caused by radiation can be reasonably contained. This will be investigated in chapter 4. Another important, but less pressing challenge is the design of the readout and the data processing of the SPAD array.
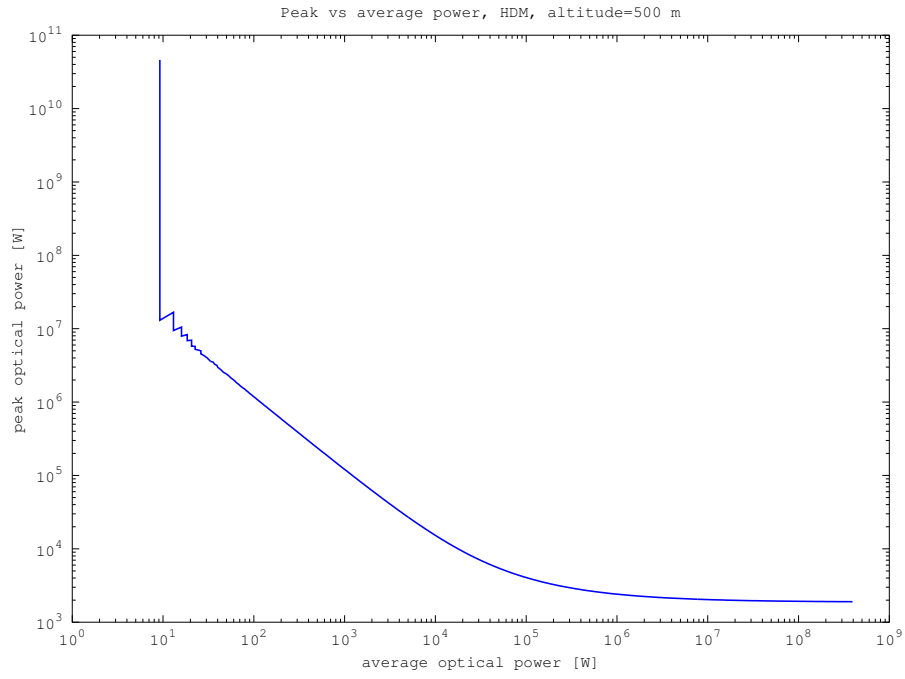
Figure 3.6: required signal photons for a given number of noise photons to meet the HDM requirements at maximum altitude

3.6 Readout

In section 3.1 two circuitry components where mentioned that are required for each SPAD: a ROIC and a TDC. While the decision on whether or not to push out the ROIC has not yet been made, section 3.3 concluded that it is necessary to push out the TDC. One other important aspect of the TDC is that it must meet the designed resolution of $50\,ps$. The proposed TDC design uses a Phase Locked Loop (PLL) to generate signals that the TDC can use to timestamp an incomming pulse. The PLL, for which a schematic is shown in fig. 3.7, locks onto an input in such a way, that both signals entering te phase detector are equal. By using a divider by X block, one can generate a signal with a frequency that is equal to x times the clock frequency. The voltage controlled oscilator is capable of generating 4 signals with 4 different phases to increase the resolution further. Figure 3.8 shows a line of TDCs connected to the PLL.
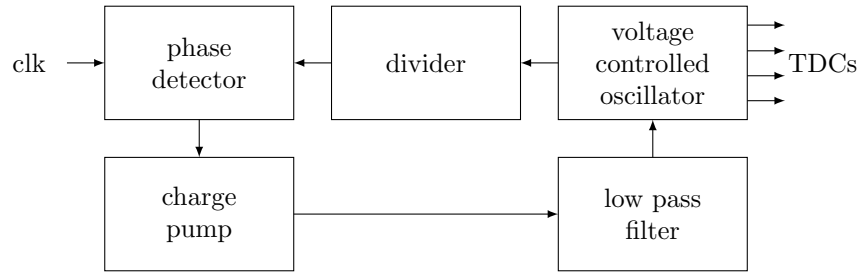

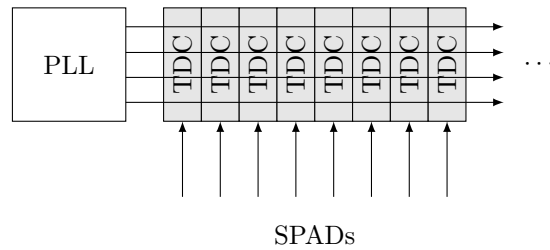Figure 3.7: schematic of phase locked loop generating signals for TDCs

Figure 3.8: TDC line connected to PLL

3.6.1 Histogram

Depending on whether an energy threshold is used or not, the data must be stored in a histogram. If no energy threshold is needed, one can simply add all the timestamps together and devide by the amount of oberserved counts to get a simple average. For more sophisticated signal processing however, more data needs to be transferred to the FPGA than just an average. One can either read every TDC value directly into the FPGA, but for the expected amount of traffic, this is not feasable. Therefore a histogram is necessary to condense the data into a smaller package without losing essential information. Considering that a histogram will be needed for every SPAD, the amount of space on the chip that the histograms can turn out to be quite large.

The amount of bits required per SPAD are dependent on the binzise, resolution and bandwidth, and can be calculated using eq. (3.1).

$$\text{bits} = \text{SPADs} \cdot \lceil \log_2(\text{binsize}) \rceil \cdot \lceil \frac{\text{bandwidth}}{\text{resolution}} \rceil \tag{3.1}$$

The next step is to investigate the limitations of these variables. First of all, the resolution is very important for both the accuracy of the device and the performance of the energy detection. The

latter has a direct relationship with the power of the laser. Lowering the resolution will effectively decrease the peak power of the signal, because the power is effectively distributed over the length of a single bin. It is assumed that the FWHM of the laser is $100\,psi$. So in order to ensure that at least one bin is exposed to the signal pulse in it's entire duration, one needs a resolution of $50\,ps$. This is also the resolution that is considered for the TDC. The binsize is dependedent on the light intensity, which will increase when approaching Europa. The bandwidth allows for some flexibility. For example, when the previous measurements where close to 8 km the device can't travel far from that altitude in the next second. The next measurement will most likely also not yield an altitude further away than the previous one. Therefore the bandwidth can be limited to some extend, and adjusted between measurements.

3.6.2   On chip signal processing

When a histogram is constructed one can decide to process the data on the chip before sending it to the FPGA. This limits the complexity of the processingstep however. It is difficult to implement a reasonable dynamic threshold for every individual histrogram, and more complex waveforms that utilize known characteristics of the signal and noise photons other than intensity becomes infeasable. However a simple circuit that only sends the largest peak, or eliminates all values before the threshold is possible.

3.6.3   connection to FPGA

The information stored in the histograms needs to be transported to the FPGA. There are several approaches that can be used to do this. The first possibility is a simple serial shift register to transport the data to the FPGA. A schematic of this is shown in fig. 3.9. This is a relatively slow solution, and the device cannot be used to receive photons during it, but this solution is very resource efficient.
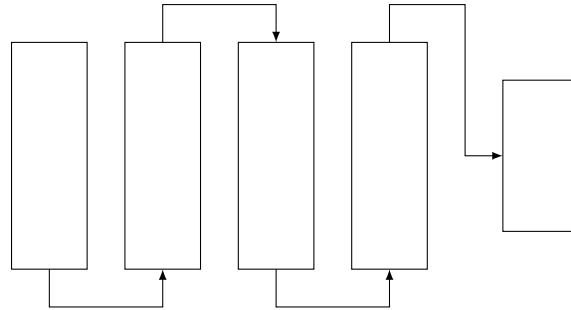

Figure 3.9: Method of transporting data from TDCs to the FPGA using a one bit serial shift register without shadowlatches

A second option is to include shadowlatches in the design. A schematic is shown in fig. 3.10. This allows the device to continue operation during readout but one needs twice as much storage to achieve this.
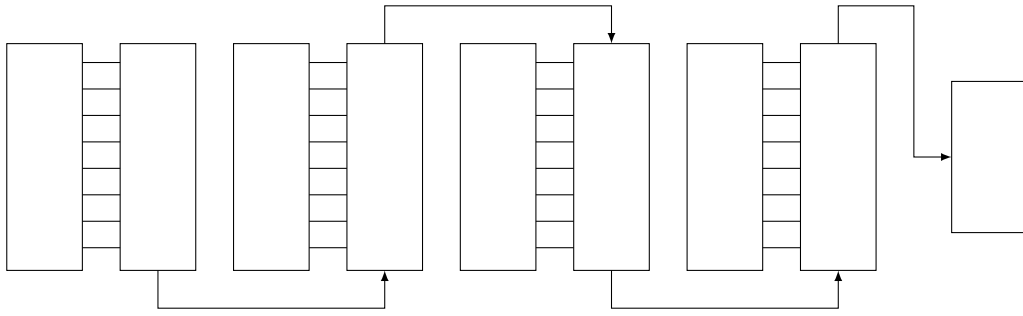
Figure 3.10: Method of transporting data from TDCs to the FPGA using a one bit serial shift register with shadowlatches

A third option is to use the same shadowlatches, but read them out in parallel. This can be done at a faster pace than the previous designs. A schematic is shown in fig. 3.11.
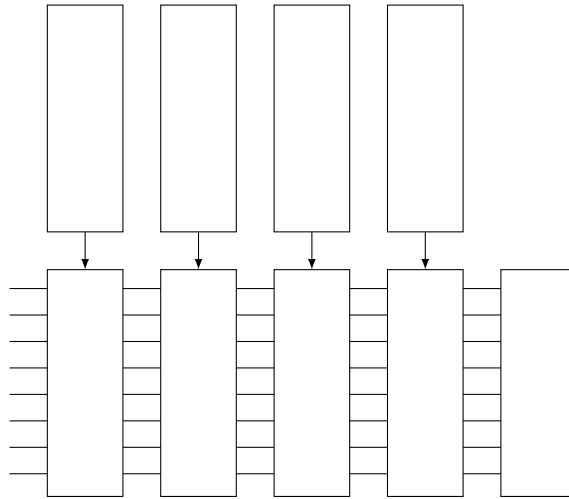

Figure 3.11: Method of transporting data from TDCs to the FPGA using a parallel shift register with shadowlatches

Considering the fact that one wants to measure for as short a time as possible, there is most likely enough time to transport the data at a small pace before the device needs to measure again. Therefore the investment into shadowlatches is not worth it. A simple serial shift register would be the best fit in this case.

Chapter 4

Radiation

One of the key challenges for deploying a sensor on the Europa Clipper is it's resilience on large amounts of radiation. The performance of the SPAD technology considered in this report when exposed to large amounts of radiation must therefore be examined.

4.1   linoSPAD

F To characterise the performance of the $0.18\,\mu s$ technology SPADs. The LinoSPAD as developed by Sammuel Burri et al. features a SPAD array of this type [2]. therefore the LinoSPAD was used to test it's resilience against radiation. Figure 4.1 shows a simple schematic of the linoSPAD. Note that the SPAD array is isolated from the readout electronics and FPGA. This is convenient for testing with a radiation beam that can be that can be directed to the SPAD array and away from the sensitive ROIC and FPGA. This layout is also useful to shield of the ROIC and FPGA using e.g. blocks of lead.
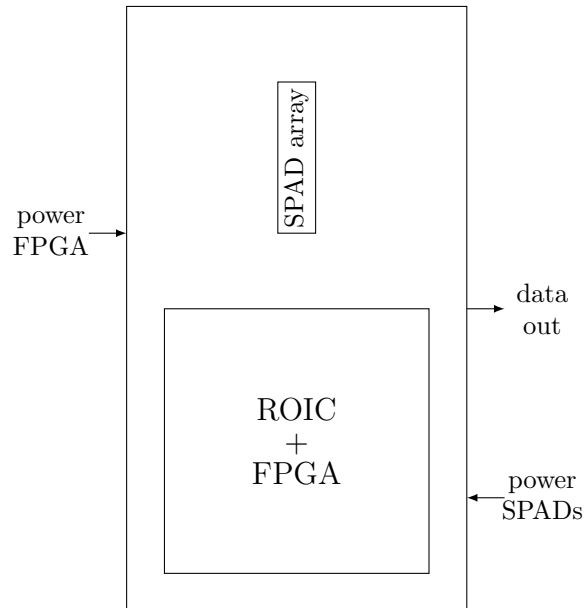

Figure 4.1: simple schematic of linoSPAD

The software used to read out the linoSPAD is programmed to count the photons for each

individual SPAD for a duration of one second and store this information in a file. This operation is called every minute.

4.2   Test setup

To characterise the performance of the linoSPAD under radiation, a test was performed in the cylcotron of the Paul Screrrer Institute (PSI) in Switzerland. The test involved proton radiation beams of both $60\,MeV$ and $10.1\,MeV$. A schematic of the setup is shown in fig. 4.2. The collimator and radiation shield have to make sure that only the SPAD array gets a large radiation dose. Figure 4.3 shows the amount of radiation that is projected onto the SPAD array as a function of time. The red dashed lines indicate the start and stop time of the $60\,MeV$ beam, and the green dashed lines indicate the start and stop of the $10\,MeV$ beam. The collimator eeds to be replaced when switching from $60\,MeV$ to $10\,MeV$ which is why the power of the SPAD array will be off for a brief time during the test. The blue line indicates the moment the power of the SPAD array is off.
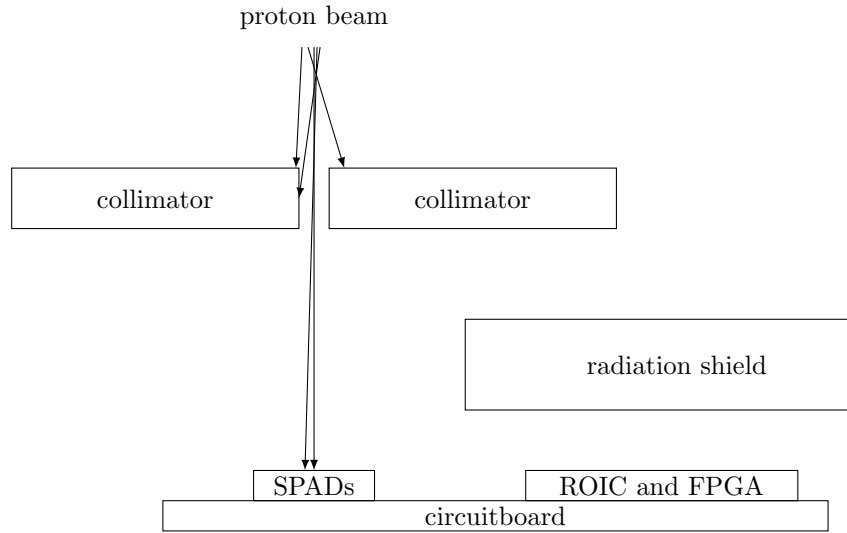

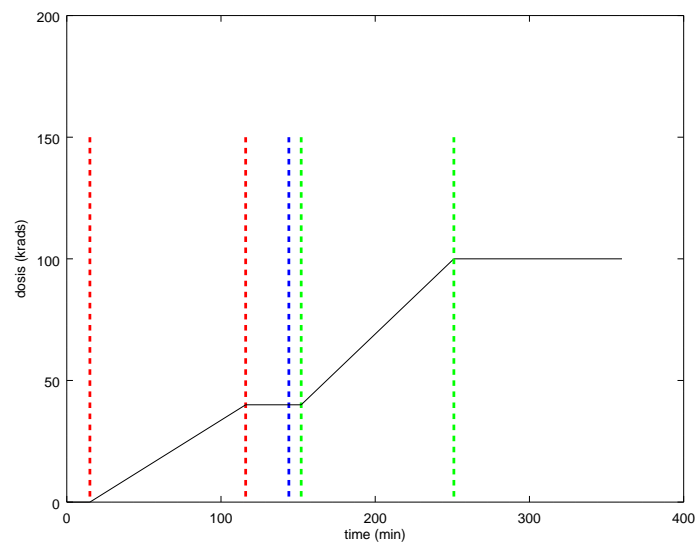Figure 4.2: schematic of radiation test setup

Figure 4.3: The accumulative dose of radiation produces by the proton radiance as a function of time

4.3 Measurements

This section shows the measurents and results obtained during the radiation experiment. Note that the linoSPAD used is a relatively noise one, in the knowledge that the device would no longer be useable for normal applications after the radtiation test.

Figure 4.4 shows the accumulative DCR of all SPADs as a function of time. The first 150 minutes are behaving as expected. The plot shows that the DCR linearly increases when the $60\,MeV$ beam is turned on with a constant intensity. After the beam is turned off, the DCR stops rising and the device starts annealing, resulting in a gradual derease of the DCR. A approximately 145 minutes, the device receives a total of 0 counts, and the reason for that is that the power on the SPAD array was briefly tunred off at that time. However the device behaves unexpectedly when the $10\,MeV$ beam is turned on. There is no change in DCR that can be observed due to the $10\,MeV$ beam, which is cotnradictory with the expectations that the $10\,MeV$ beam would cause more damage than the $60\,MeV$ beam. Another interesting event is that at approximately 165 minutes, $25\,\%$ of the SPADs no longer detect counts. Figure 4.5 shows the same graph, but with the $25\,\%$ defect SPADs removed. Here one can see that the other SPADs are not at all affected by the $10\,MeV$ beam and continue annealing. At approximately 240 minutes the entire sensor stops communicating, 10 minutes before the beam is turned off.
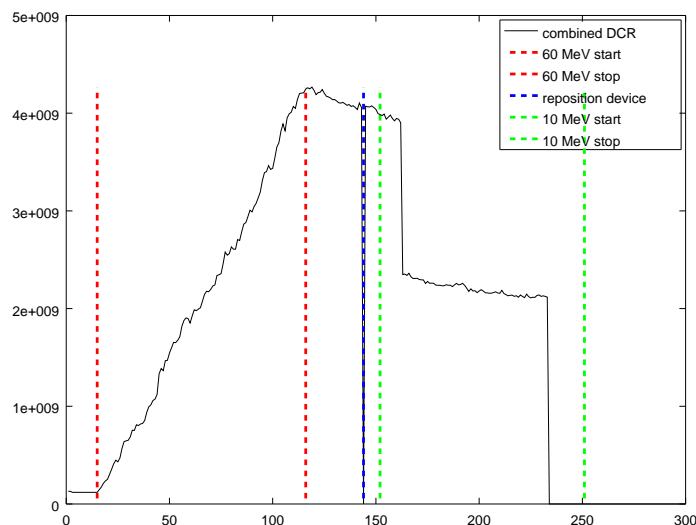

Figure 4.4: The amount of DCR for the sum of all SPADs combined as a function of time

Figure 4.6 shows the accumulative number of counts for individual SPADs. This plot illustrates that the contribution in DCR varies wildly across different SPADs. It also shows that the second half of the SPADs seem te behave at a much lower count than the first half, which is something that needs to be looked at.

Figure 4.7, fig. 4.8 and fig. 4.9 show the individual DCR as a function of time for three SPADs in the high, mid and low segment respectively. The segments are sorted by how much counts a SPAD accumulated over the course of the entire test. Note that the individual SPADs don't show the same trend as the sum of all SPADs. The individual SPADs get damaged at arbitray points in time, and anneal at a certain point in time.

Figure 4.10 shows the spread of DCR for single SPADs at different points in time. The behavior is consistent with the results shown in fig. 4.4. Note that after approximately 165 minutes $25\,\%$ of the SPADs stop working, which is the reason why the black line starts at $25\,\%$.

The results of the test are in line with until the 150 minute mark, but afterwards the reaction to the $10\,MeV$ beam is odd. The break down at 165 minutes and 250 minutes indicate damage in the readout circuit. This is a feasible explanation for the events as it is known that the $10\,MeV$ can be
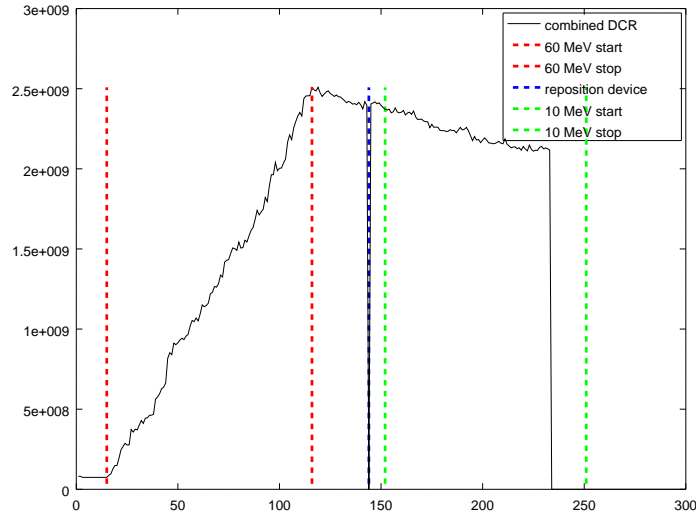
Figure 4.5: The amount of DCR for the sum of 75 % of SPADs combined as a function of time. The left-out 25 % are the SPADs that broke down at the 165 minute mark

very damaging to these types of cicruitry. This would mean that the protection provided for the ROIC and FPGA where insufficient. There are two possible explanations for the observation that the SPADs are not affected by the $10\,MeV$ beam that will be listed here. The first explanation, is that the SPADs at this particular $0.18\,\mu m$ technology are not affected by the $10\,MeV$ as opposed to their $0.35\,\mu m$ counterpart. The second explanation is that something went wrong during the setup of the $10\,MeV$ beam test, which caused the beam to aim for the ROIC and FPGA instead of the SPAD array.

Considering only the effect of the $60\,MeV$ beam, and especially the behavior observed in fig. 4.5, show a very interesting trend where the change in DCR seems to be a linear relationship with the amount of radiation it is exposed to. Both the periods between 10 and 120 minutes, and between 120 and 240 minutes show a very constant slope. This means that not only the amount, but also the time over which the radiation dose is accumulated graetly affects the DCR of the device. This property should be further investigated and compared to the circumstances at Europa.
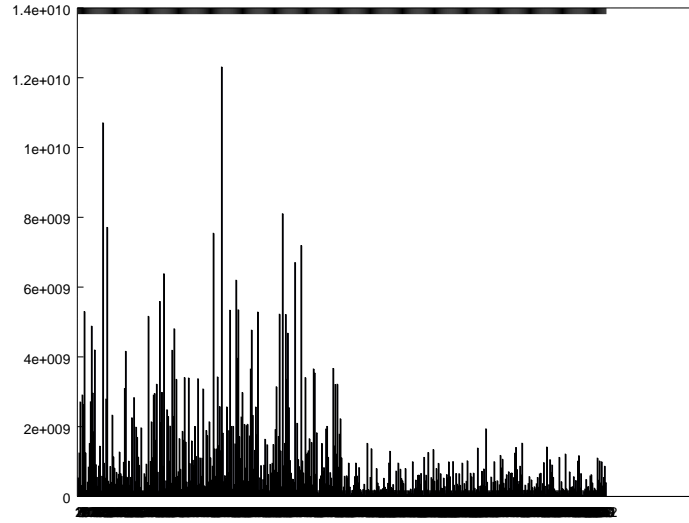
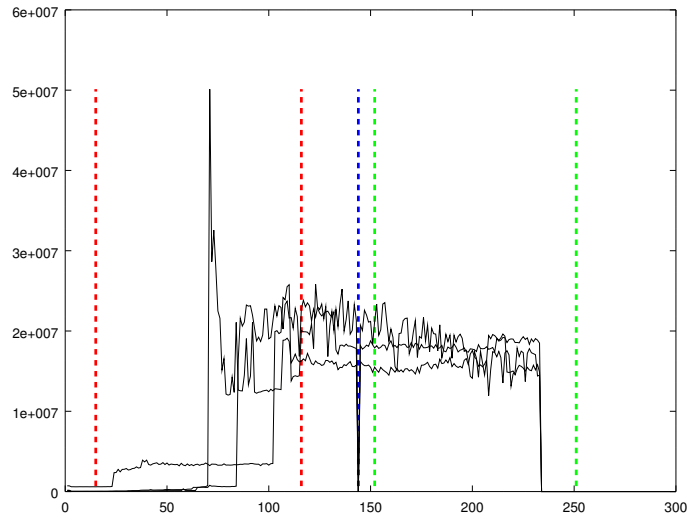Figure 4.6: accumulative number of counts for the entire experiment for individual SPADs

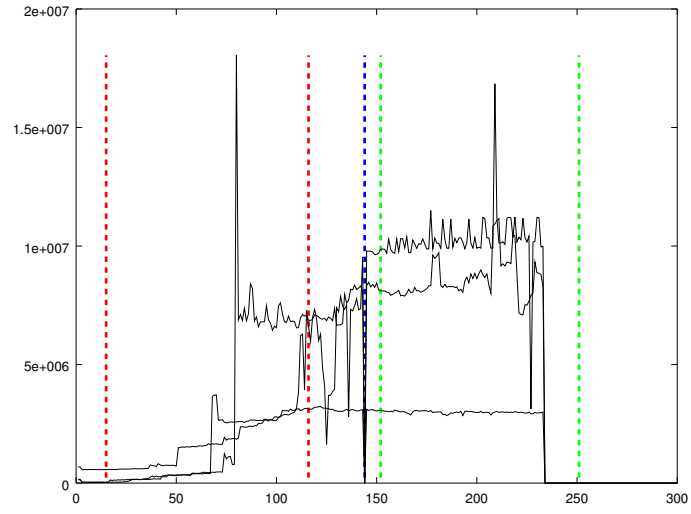Figure 4.7: three SPADs from that are in picked from the 33 % SPADs with the highest contribution to noise

Figure 4.8: three SPADs from that are in picked from the 33 % SPADs with the most average contribution to noise
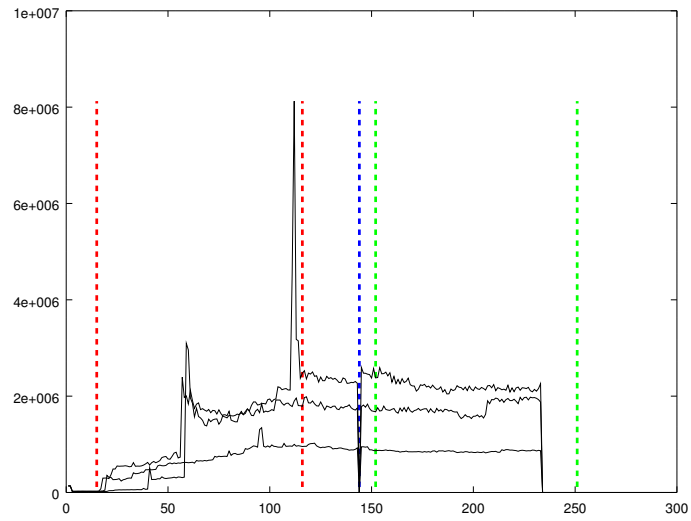

Figure 4.9: three SPADs from that are in picked from the 33 % SPADs with the lowest contribution to noise
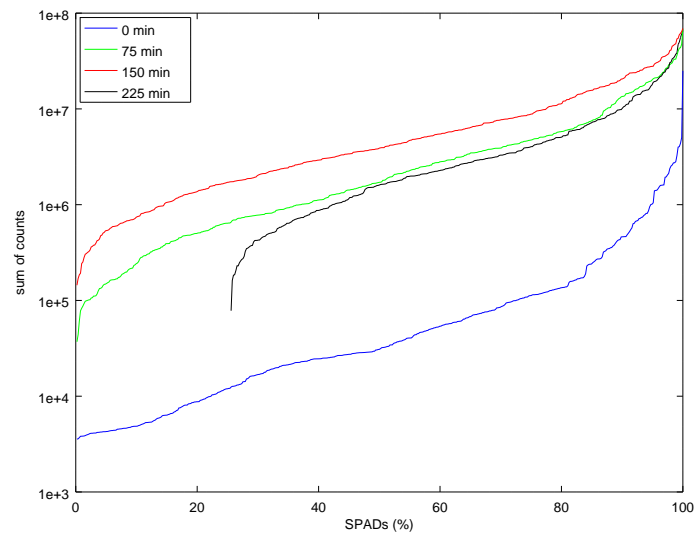
Figure 4.10: distribution of DCR over individual SPADs at different time frames. After the 165 minute mark 25 % of SPADs stop working, which is why the black line starts later at 25 %

4.4 Comparison

The next step is to compare the results from the measurements obtained in this experiment, and results from precious experiments. An overview of the performance of this device when compared to another with 3.5 μm technology is shown in table 4.1. The measurements of the compraed device are based on the work of Carrara et al. [3] and Burri [1]. A first observation is that the DCR of the new measurements show DCR measurements that are way higher than the other devices. There are three possible explanations for this. Firstly, in the knowledge that the device would be unusable after the test, a relatively noise device was used. Secondly, the SPADs used in the new device have a lot more active area that is capable of receiving photons, but also receive radiation, generate DCR and traps. A third possibility is an error in the software where the DCR does not match the read-out values. consistent. Also the effect of radiation is different. The old measurements show an increase of rougly 50 times the DCR, while the new test shows an increase of 250 times.

Table 4.1: Comparison of DCR for different radiation tests. The bold entry is the one described in this report

proton energy	dose	initial DCR	final DCR	DCR after annealing (anneal time)
10 Mev	40 krad	140	6298	3884 (10 days)
60 Mev	40 krad	142	6290	1299 (21 days)
60 Mev	**40 krad**	$\mathbf{2 \cdot 10^4}$	$\mathbf{5 \cdot 10^6}$	$\mathbf{4 \cdot 10^6 (2\ hours)}$

There are two considerations to be made on these observations. The first one is to redo the measurements to confirm them. The measurements don't line up with the expectations, especially for the $10\,MeV$ beam. A second option is to not use the technology used in the experiment but another one that is more resilient against radiation. The DCR and sensitivity to radiation are a function of active area, which means that reducing this will improve the DCR. For example a deliberatly small active area with microlenses could potentially increas the resilience against radiation.

4.5 Effect of radiation on performance

Now that the results of the radiation tests are in, it is worth revisisting the calculations performed in section 3.4 and section 3.5. In these sections, the DCR was so low that it was of absolutely no consequence, and completely dominated by the background noise. Figure 4.10 however, shows that with a dose of $40\,krad$ applied in approximately 2 hours, the average DCR can rise to approximately 10^7 counts/s. This means that for a large amount of radiation damage, the DCR starts to dominate over the background noise. Now the expected amount of background noise is expected to be $500\,krad$ as is listed in section 1.1. Now assuming that all this radiation is $60\,MeV$ radiation build up with similar conditions as during the radiation test, that the relationship between dose and DCR stays linear as observed, and assuming that about half of the damage is healed over time due to annealing, one can make a loose estimation about the required peak and average power of the laser to meet the resolution requirements.

The average amount of DCR after $40\,krad$ of radiation is 10^7counts/s. Extrapolating this number to the assumptions made previously on gets a $6.25 \cdot 10^8$ counts/s. The resulting peak and average optical laser power are calculated below.

$$P_{peak} = \frac{10 \cdot DCR}{PPS_S}$$
$$= 33\,kW$$
$$P_{av} = P_{peak} \cdot FWHM$$
$$= 3.3\,\mu W$$

4.6 Possible improvements

Finally there are several ways that the resilience against radiation could be improvement. A first improvement could be a shield in front of the sensor that can be removed when the sensor is desployed. A second improvement could be to look in the FPGA for unusually high counts among the SPADs to filter out the SPADs who are damaged the most. This solution could mean however that not all pixels of the target image can be produced, because some data is missing.

Chapter 5

Recommendations

This section contains the recommendations based on findings described in this report. The recommendations will be structured based on the rest of the document.

5.1 Altimetry Mode Recommendations

The calculations in chapter 2 show that the Altimetry mode requires a focussed laser and focussed observation in order to be resource efficient. This might be achieved by turning of SPADs during the altimetry mode and sending a focussed laser pulse. The performance can be further improved by using an intensity threshold to filter noise. Also the period of the laser, and the measurement time should be at least the maximum time of flight which is $53.3\,\mu s$. There is no need for complex optics. The Altimetry Mode is less critical than the Hazard Detection Mode.

5.2 Hazard Detection Mode

Considering the required resolution and the size of a SPAD, it is not feasable to have a SPAD for every pixel. Therefore a 2048×8 grid is proposed. Depending on the achievable peak laser power, it is advantages to use very few pulses per measurement. A histogram with an intensity threshold is recommended to keep the required average and peak power within proportions. The histograms should be read out to the FPGA using a single bit serial shift register, where the intensity threshold is applied. The option to use a more soffisticated measurement method is worth consideration.

5.3 Radiation

The results from the radiation test are not in line with the expectation which means that extra investigation and confirmation is necessary to draw final conclusions about the technology. If the measured performance is reprentative for the performance it might be necessary to deliberately decrease the photon sensitivity of the chip to decrease the DCR and resilience against radiation of the SPADs. It might be worth considering using an older SPAD technology that has a proven relience against radiation instead.

Appendix A

Double frequency sampling

Two frequency sampling

The measurement time based on The maximum pulse frequency can then be calculated using eq. (A.1).

$$t_{TDC} = ToF \mod T_{pulse} \tag{A.1}$$

$$ToF = t_{TDC} + k \cdot T_{pulse} \qquad\qquad k \in \mathbb{N} \tag{A.2}$$

where t_{TDC} is the measurement of the TDC, ToF the time of flight, and T_{pulse} the time period of the laser pulses. The returned answer is related to ToF as shown in eq. (A.2). There will be ambiguity when it is possible for T_{pulse} to be smaller than ToF. The maximum frequency without ambiguity can be calculated using eq. (A.3).

$$f_{pulse} = \frac{1}{t_{round}} = \frac{c}{2r} \tag{A.3}$$

To solve the ambiguity problem one can make measurements in two different frequencies. In the first half of the measurement, the pulses will have a period t_1, and in the second half a smaller period t_2. These two different measurements can first be used to determine the large scale ToF, and then the measurements can be combined to get a high accuracy to accompany that. The difference between the different measurements are in steps of equal distance. The size of these steps can be calculate with **??**.

$$t_{step} = t_1 - t_2 \tag{A.4}$$

Given measurements t_1 and t_2 one can calculate the time of flight using eq. (A.6).

$$t_{1-2} = (t_1 - t_2) \mod T_2 \tag{A.5}$$

$$ToF = \frac{t_{1-2}}{T_2 - T_1}T_1 + \frac{t_1 + t_2 - t_{1-2}}{2} \tag{A.6}$$

where t_1 and t_2 are the timestamp measurements for f_1 and f_2 respectively. t_{1-2} is the modulus of the time difference between t_1 and t_2.

Bibliography

[1] Samuel Burri. *Challenges and Solutions to Next-Generation Single-Photon Imagers.* PhD thesis, Ecole Polytechnique Federale de Lasusanne, 2064.

[2] Samuel Burri, Harald Homulle, Claudio Bruschini, and Edoardo Charbon. Linospad: a time-resolved 256×1 cmos spad line sensor system featuring 64 fpga-based tdc channels running at up to 8.5 giga-events per second. In *SPIE Photonics Europe*, pages 98990D–98990D. International Society for Optics and Photonics, 2016.

[3] Lucio Carrara, Cristiano Niclass, Noemy Scheidegger, Herbert Shea, and Edoardo Charbon. A gamma, x-ray and high energy proton radiation-tolerant cis for space applications. In *2009 IEEE International Solid-State Circuits Conference-Digest of Technical Papers*, pages 40–41. IEEE, 2009.

[4] Juan Mata Pavia, Martin Wolf, and Edoardo Charbon. Measurement and modeling of microlenses fabricated on single-photon avalanche diode arrays for fill factor recovery. *Optics express*, 22(4):4202–4213, 2014.